A 3D-FSS-Based and Front-Feeding Shared-Aperture Base Station Antenna for 5G Mobile Communications

Yejun He, *Senior Member, IEEE*, Guodong Liao, *Graduate Student Member, IEEE*, Zhou He, and Zhi Ning Chen, *Fellow, IEEE*

***Abstract*—This article presents a novel compact low-profile dual-polarization base station antenna (or unit cell) designed for 5G mobile communications, which does not require additional baffles. This proposed base station antenna comprises a lower band (LB) element (2.0–2.6 GHz) and four higher band (HB) elements (2.7–3.4 GHz). A new 3-D frequency-selective surface (3D-FSS) is used in the LB element to minimize mutual coupling in this unit cell. Since the operating frequency bands within the HB elements and the LB element are adjacent, the coupling between the elements is also a concern. Meanwhile, this article also proposes a unique front feeding and the addition of the extended metal arms (EMAs) to hinder the coupling current and achieve effective decoupling. The simulated and measured results show that our unit cell reaches a high gain in the LB element (8.3 ± 0.5 dBi), with an average increase of 1.1 dBi using front feeding compared to conventional balun feeding, and a high gain in the HB element (13 ± 0.7 dBi). The LB and HB elements exhibit the high port isolation of more than 20 dB, the high cross polarization of more than 25 dB, and stable radiation patterns, fulfilling the requirements for dual-band 5G base station antennas.**

***Index Terms*—Adjacent frequency decoupling, base station antenna, dual polarization.**

I. Introduction

THE rapid development of fifth-generation communication systems (5G) has led to increased interest in dual-frequency dual-polarization base station antennas. To accommodate user needs, 5G must coexist with existing 4G systems, but the deployment of earlier base station antennas limits available space for 5G base station antennas. Currently, the trend is toward shared-aperture multifrequency-band antenna arrays, usually consisting of many unit cells [1], which integrate 5G antennas with those of previous generations within the same radiation aperture, offering cost and space efficiency. Key design considerations include the frequency ratio and aperture reuse efficiency. Configurations for shared-aperture antenna arrays include side-by-side, embedded, stacked, staggered [2], and structural reuse layouts. In the parallel layout, subarrays for different frequency bands are placed side by side. However, this method has low space utilization and requires significant spacing to reduce coupling, resulting in a larger volume requirement.

The embedded layout of shared-aperture antennas [3], [4], [5], [6] involves embedding one or more higher band (HB) elements within a lower band (LB) element. Antenna arrays operating at different frequencies can function independently. This approach effectively minimizes the radiation shielding effect of the LB element on the HB element while meeting the spacing requirements of various antenna arrays. As a result, it achieves significant space-saving benefits.

The stacked layout of shared-aperture antennas [7], [8], [9], [10] involves multiple antenna elements that operate in different frequency bands and are stacked together to cover these bands effectively. Typically, the HB element is positioned above the LB element, which has a larger physical size. This arrangement prevents the LB element from obstructing the HB element. While this layout allows for a more compact design, it may also lead to an increase in the overall antenna profile.

The staggered layout of shared-aperture antennas [11], [12], [13], [14], [15] involves staggering LB and HB elements to maximize space utilization. However, both the embedded and stacked configurations have limitations based on the frequency ratio between LB and HB elements.

The shared-aperture antenna with structure-reuse technology enables antennas of different frequency bands to share the same aperture by reusing the antenna structure designed for a specific frequency band. For instance, the same radiator can be utilized multiple times to cover various frequency bands within the same aperture, thus saving significant space. However, this design approach is often more complex. The shared-aperture antenna encounters significant design challenges in complex electromagnetic environments due to coupling inter-

Received 15 April 2025; revised 31 August 2025; accepted 8 September 2025. Date of publication 29 September 2025; date of current version 18 December 2025. This work was supported in part by the National Key Research and Development Program of China under Grant 2023YFE0107900, in part by the National Natural Science Foundation of China under Grant 62071306, and in part by the Key Program of Shenzhen Natural Science Foundation under Grant JCYJ20241202124219023. *(Corresponding author: Yejun He.)*

Yejun He and Guodong Liao are with the State Key Laboratory of Radio Frequency Heterogeneous Integration, Sino-British Antennas and Propagation Joint Laboratory of Ministry of Science and Technology of China, Guangdong Engineering Research Center of Base Station Antennas and Propagation, Shenzhen Key Laboratory of Antennas and Propagation, College of Electronics and Information Engineering, Shenzhen University, Shenzhen 518060, China (e-mail: heyejun@126.com; 2664814941@qq.com).

Zhou He is with the Department of Mechanical Engineering, University of Maryland, College Park, MD 20742 USA (e-mail: zhe12@umd.edu).

Zhi Ning Chen is with the Department of Electrical and Computer Engineering, National University of Singapore, Singapore 119077 (e-mail: eleczn@nus.edu.sg).

Digital Object Identifier 10.1109/TAP.2025.3613502

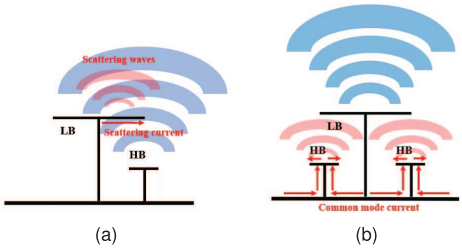

Fig. 1. (a) Scattering interference. (b) Common-mode interference.

ference. This interference can be categorized into two main types: heterodyne-frequency coupling interference, which occurs between antennas of different frequency bands, and co-frequency coupling interference, affecting antennas within the same frequency band. Coupling interference can result in impedance mismatch, reduced isolation, signal attenuation, and cross-interference, thereby degrading signal stability and quality. It can also diminish antenna performance by reducing gain and distorting radiation patterns, impacting coverage range and quality. To address these issues, appropriate decoupling strategies must be implemented. Heterodyne-frequency coupling interference can be further classified into scattering interference and common-mode interference, as shown in Fig. 1, each requiring specific decoupling technologies to mitigate their effects.

Currently, some methods such as adding frequency-selective surfaces (FSSs) [16], [17] and chokes [14], [18], [19], [20], [21] are employed to address scattering interference. To tackle common-mode interference, a metasurface has been introduced beneath the HB element to form a band-stop filter [22]; however, this significantly increases the space occupied by the antenna. Additionally, the insertion of a metal column at the end of the HB element's radiation surface has been proposed for "path extension" to mitigate common-mode interference [23]. Unfortunately, this approach raises both the manufacturing cost and complexity of the antenna.

In this article, we present a 5G base station antenna based on a 3D-FSS and a front-feeding design, which achieves a low profile, minimal coupling, and a compact footprint. The antenna height is only 30 mm, adequately meeting the performance requirements for 5G base stations and offering an effective and reliable implementation plan for current base station construction.

The main contributions of this article are as follows.

1) A novel dual-bandwidth, dual-polarization staggered shared-aperture base station antenna (unit cell) is designed, featuring closely spaced operating frequency bands. This design eliminates the need for additional baffles to achieve high port isolation and resolve coupling issues.
2) The implementation of 3D-FSS effectively addresses scattering interference when the frequency bands of the antennas are very close (adjacent frequency). Such low profile and proximity of elements within the unit cell are first addressed and operate in adjacent frequencies.

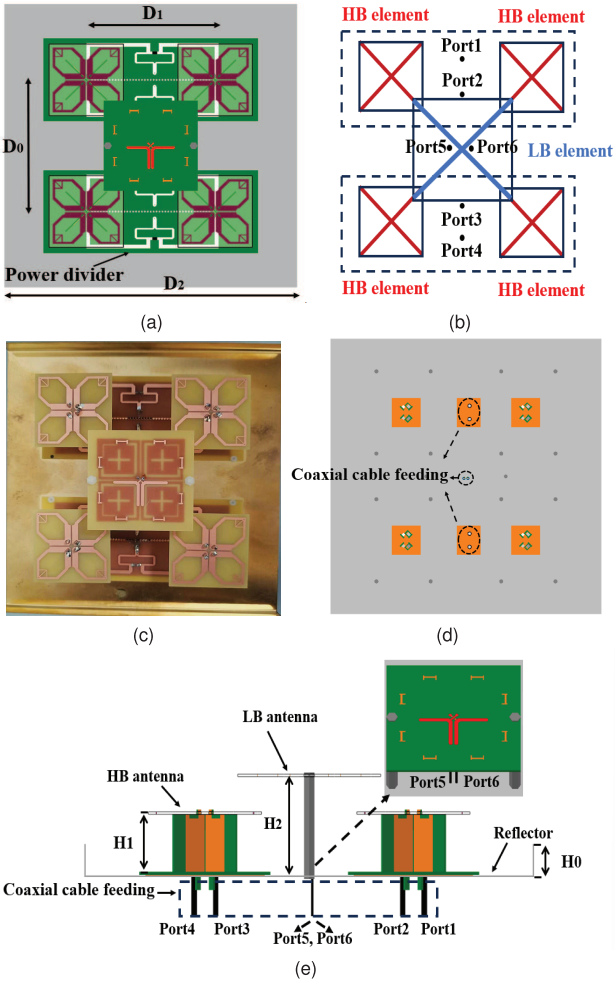

Fig. 2. Configuration of the proposed adjacent frequency base station antenna (unit cell). (a) Top view. (b) Port number assignment. (c) Practical antenna (top view). (d) Bottom view. (e) Side view.

3) The front-feeding structure effectively mitigates common-mode interference without increasing the area occupied by the antenna and without necessitating complex manufacturing processes, which helps to reduce costs.

The rest of this article is organized as follows. Section II the overall structure of this unit cell, describes the 3D-FSS structure with its working principle within the LB element, and the front-feeding structure that effectively realizes the band-stop filter of the HB antenna to the LB antenna and explains its working principle. The simulation of the proposed antenna array is designed in Section III with an experimental verification. The conclusion is drawn in Section IV.

II. Antenna Design

A. Antenna Geometry

The top view, port number assignment, practical antenna top view, bottom view, and side view of the proposed adjacent frequency band base station antenna (unit cell) are shown in Fig. 2(a)–(e); an LB element is located in the center and it adopts the 3D-FSS to make it electromagnetically transparent to the adjacent frequency HB elements. The four HB elements

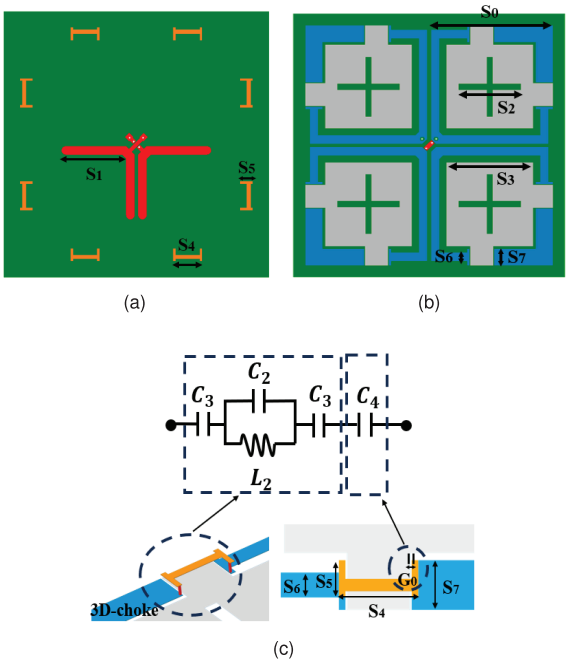

Fig. 3. Configuration of the proposed LB element. (a) Top view, (b) bottom view, and (c) 3-D choke.

are located at the four corners of the unit cell, powered by a Wilkinson power divider with a shared-aperture design to save space. The size of the reflector is $D_2 \times D_2$, and the height of the LB and HB elements is H_1 and H_2, respectively. The LB element operates from 2.0 to 2.6 GHz, and the HB elements operate from 2.7 to 3.4 GHz. The distances D_0 and D_1 can be selected to avoid the generation of grating lobes.

Based on the theoretical analysis presented in Section II-C, the dipole arm form of the LB element was determined. Furthermore, due to the excellent adjacent frequency band decoupling capability of 3D-FSS, the designed base station antenna (unit cell) has a small overall cross section, eliminating the need for additional decoupling structures.

By adding a power divider to the HB element to improve system integration, the conventional feeding structure will produce severe common-mode interference. Therefore, we use a special band-stop filter design based on Section II-D in the HB feeding structure to mitigate common-mode interference. Excellent simulation and measurement results are obtained, proving its applicability in actual large-scale base station antenna arrays.

B. Design of the LB Element

The new type 3D-FSS structure is shown in Fig. 3. The patches are all printed on the FR4 with a dielectric constant of 4 and a thickness of 0.762 mm, as shown in Fig. 3(a) and (b).

The evolution of the dipole arm end design from S_6 to S_7 aims to expand the bandwidth of the LB element as shown in Fig. 3(c). As the width of the dipole arm changes, the impedance also varies, which helps to reduce the coupling current. To further mitigate the coupling current generated on the LB dipole arm due to the excitation of the HB element,

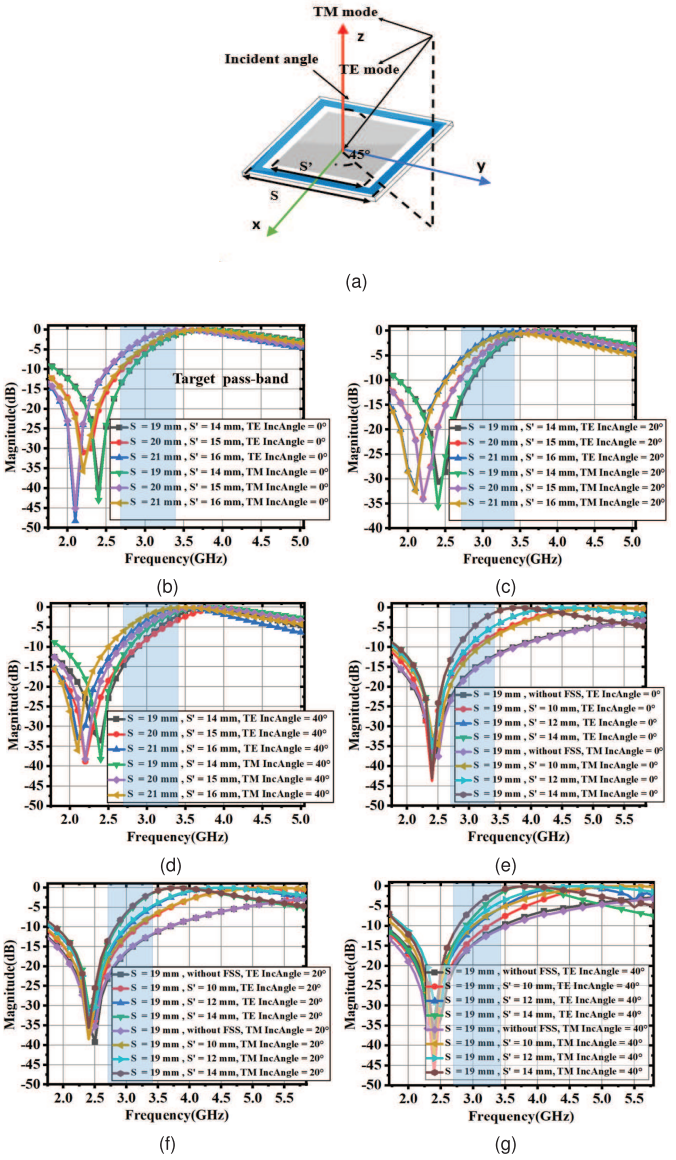

Fig. 4. Simulated transmission coefficients of (a) FSS unit. TE/TM mode under (b) normal incidence, (c) 20° incidence, (d) 40° incidence, (e) normal incidence, (f) 20° incidence, and (g) 40° incidence.

we consider adding a 3-D choke into the dipole arm as shown in Fig. 3(c). However, since the 3-D choke can cause a frequency deviation in the resonance point of the LB antenna, careful selection of its placement is crucial. To ensure optimal performance of the LB element, the 3-D choke has been positioned near the impedance change point at the end of the dipole arm.

Nevertheless, this adjustment alone is insufficient to address the shadowing effect observed in this adjacent frequency band antenna unit cell. We can clearly see that embedding the rectangular parasitic patches in the dipole arm to form the FSS can significantly change the passband frequency and make it electromagnetically transparent to the proposed HB elements [16], [17], but at the same time, the passband is also limited by the size of the FSS, as shown in Fig. 4(a)–(c). When we obtain the target passband, we need to greatly increase the

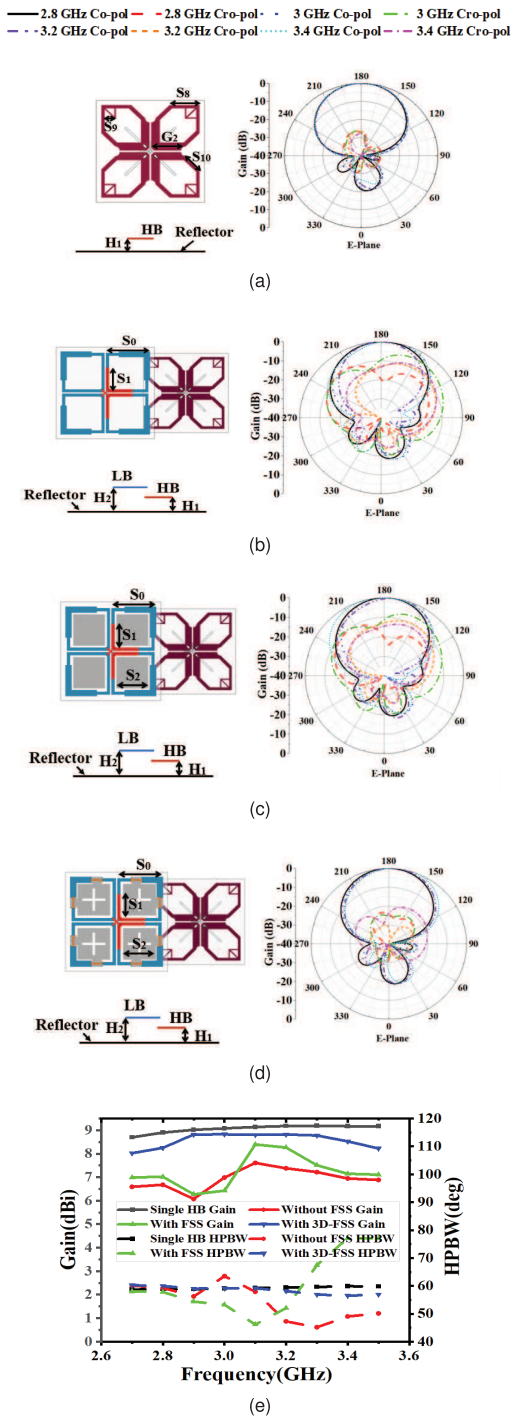

Fig. 5. Radiation patterns for HB element with different decouple structures. (a) Single HB element, (b) HB–LB elements without decoupling structure for LB element, (c) HB–LB elements with FSS for LB element, (d) HB–LB elements with 3D-FSS for LB element, and (e) representative simulated gain curve and HPBW.

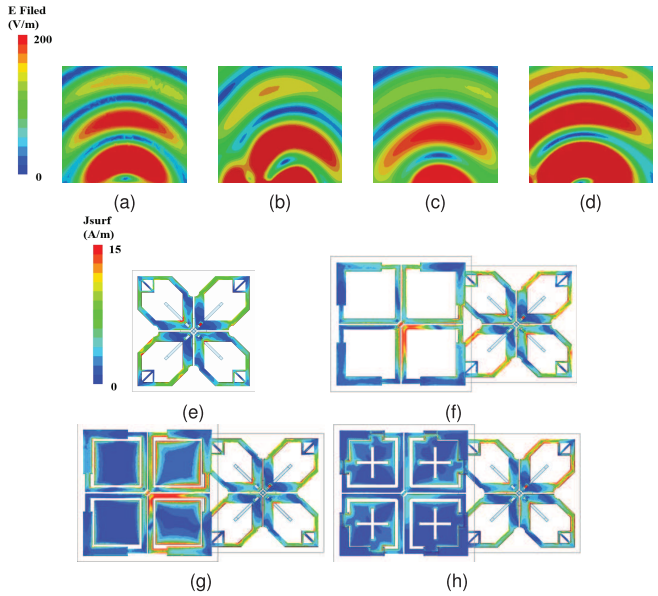

Fig. 6. Simulated E-field distributions for HB element at 3.2 GHz. (a) Single HB element without decoupling structure, (b) HB–LB elements without decoupling structure, (c) HB–LB elements with FSS, and (d) HB–LB elements with 3D-FSS. Simulated surface current distributions for LB and HB elements at 3.2 GHz. (e) Single HB element without decoupling structure, (f) HB–LB elements without decoupling structure, (g) HB–LB elements with FSS, and (h) HB–LB elements with 3D-FSS.

length of S and S′ in proportion, which will take up a lot of space.

Therefore, we specifically design the 3D-FSS structure. It can ensure that the target passband is achieved without increasing the space occupied by the antenna unit. The specific part of the parasitic rectangular patch added in the dipole arm is expanded to fill the part of the dipole arm that is vacant due to the introduction of the 3-D choke. Cross-shaped slots are adopted to expand the transmission bandwidth slightly.To demonstrate the performance advantages of the designed 3D-FSS, we conduct verification experiments, as shown in Fig. 5. In Fig. 5(a), the radiation pattern of a single HB element is presented. Fig. 5(b) shows the scenario in which the HB–LB elements are without a decoupling structure for the LB element, resulting in a distorted radiation pattern for the HB element. In Fig. 5(c), we can see that when the antenna dipole arm length S_0 is 19.7 mm, adding a rectangular parasitic patch to the dipole arm is not enough to achieve an FSS that meets the target passband. However, as shown in Fig. 5(d), the HB–LB elements utilizing the 3D-FSS structure for the LB element effectively resolve this issue, restoring the radiation pattern.

Utilizing a 3D-FSS for decoupling adjacent frequency antennas yields improved results. This approach not only significantly improves cross-polarization within the target frequency band but also enhances the consistency of the HB element.

Fig. 6 shows the electric field and current distribution in various states, which helps to understand the effectiveness of 3D-FSS decoupling. Fig. 6(a) shows the electric field distribution of a single HB element. Fig. 6(b) and (e) shows that when the HB–LB elements are without a decoupling structure for the LB element, the LB element will generate a strong coupling current, the electric field of the HB element becomes distorted, adversely affecting antenna radiation. Fig. 6(c) and (f) shows that when the HB–LB elements adopt the FSS structure for the LB element, the coupling current is slightly reduced and the radiation pattern is partially restored,

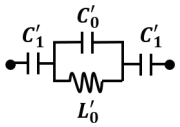

Fig. 7. Equivalent filter circuit of 3-D choke.

but due to the limitation of S_0 length, it is difficult to achieve electromagnetic transparency in the target frequency band. In Fig. 6(d), the HB–LB elements utilizing the 3D-FSS structure for the LB element effectively address this issue, allowing the electric field to return to levels similar to those observed in Fig. 6(a).

C. Principle of 3D-FSS

The equivalent circuit model of the 3D-FSS is shown in Fig. 7. It consists of a parallel-resonant circuit at HB (composed of L_0' and C_0') and a series resonant circuit at LB (composed of two additional capacitors C_1') [14].The above conditions satisfy

$$2\pi j f_H C_0' + \frac{1}{2\pi j f_H L_0'} = 0 \tag{1}$$

$$\frac{1}{2\pi j f_L C_1'} + \frac{1}{2\pi j f_L C_0' + \frac{1}{2\pi j f_L L_0'}} = 0 \tag{2}$$

where f_H denotes the open-circuit frequency point of the HB and f_L represents the short-circuit frequency point of the LB. At higher frequency bands, the induced current is effectively open-circuited as it passes through the 3-D choke. In contrast, at lower frequency bands, the current is nearly short-circuited, which has a minimal impact on the lower frequency operation of the antenna.

Next, we consider how to adjust the passband to the target frequency band while keeping the dipole arm length unchanged. The square rings from Case 1 to Case 4 have a uniform width of 1.4 mm, the same as S_6.

The evolution of 3D-FSS will be described in Fig. 8, where Z_a represents the wave impedance in free space and Z is determined by the geometric dimensions S and dielectric properties. In Fig. 8(a), the dipole arm of the LB element is equivalent to an inductor L_0 and a capacitor C_0 in series. The LC series circuit provides a band-stop response, which shows that the traditional loop antenna has a serious hindering effect on the HB element. In Fig. 8(b), we add rectangular patches to the dipole arm to shape the FSS. We can see in Fig. 4(e)–(g) that when the size of the square ring remains unchanged and the internal rectangular patch is enlarged, it is found that while the transmission zero point on the left remains unchanged, the passband shifts to the left, indicating that a new resonance is introduced, so the equivalent circuit diagram changes from Case 1 to Case 2. Case 3 of adding 3D-FSS alone in the dipole arm can be calculated from its ABCD matrix according to the provided conversion formula and can be described as

$$\begin{bmatrix} A & B \\ C & D. \end{bmatrix} = \begin{bmatrix} 1 & 0 \\ \frac{1}{Z_F} & 1. \end{bmatrix} \times \begin{bmatrix} \cos\beta h_1 & jZ\sin\beta h_1 \\ \frac{j\sin\beta h_1}{Z} & \cos\beta h_1 \end{bmatrix}$$

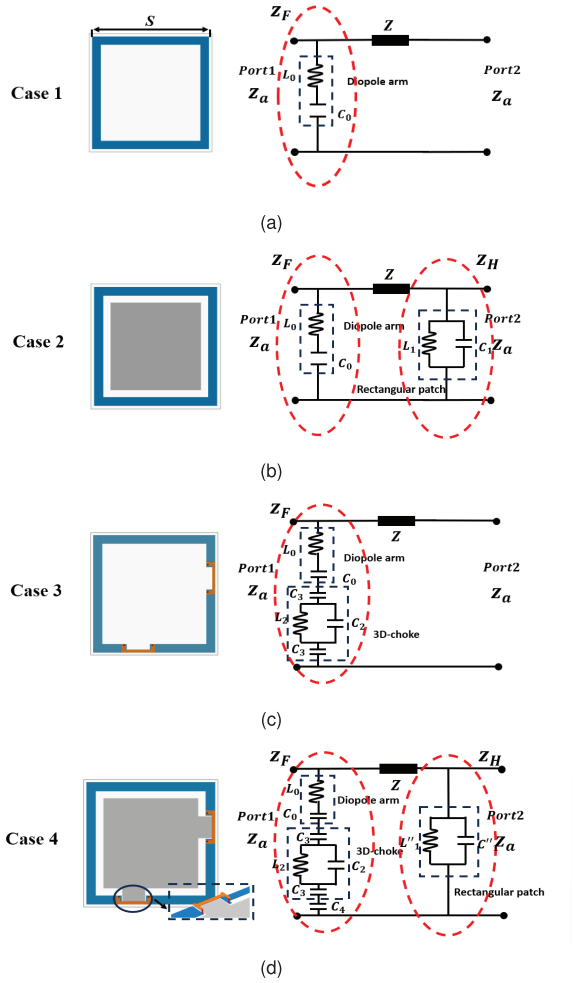

Fig. 8. Equivalent filter circuit for different filter units. (a) Case 1: dipole arm, (b) Case 2: dipole arm with rectangular parasitic patch, (c) Case 3: dipole arm with 3-D choke, and (d) dipole arm with 3-D choke and special parasitic patch.

$$= \begin{bmatrix} \cos\beta h_1 & jZ\sin\beta h_1 \\ \frac{j\sin\beta h_1}{Z} + \frac{\cos\beta h_1}{Z_F} & \frac{jZ\sin\beta h_1}{Z_F} + \cos\beta h_1 \end{bmatrix} \tag{3}$$

$$|S_{21}| = \left| \frac{2}{A + \frac{B}{Z_a} + CZ_a + D} \right| = \left| \frac{2}{\cos(\beta h_1)\left(2 + \frac{Z_a}{Z_F}\right) + j\sin(\beta h_1)\left(\frac{Z}{Z_a} + \frac{Z_a}{Z} + \frac{Z}{Z_F}\right)} \right| \tag{4}$$

where $\beta = 2\pi f/c$ is the phase constant, f is the operating frequency, c is the propagation speed of electromagnetic waves in free space, and h_1 is the transmission electrical length. First, we assume

$$M = 2 + \frac{Z_a}{Z_F}$$
$$N = \frac{Z}{Z_a} + \frac{Z_a}{Z} + \frac{Z}{Z_F}$$
$$\theta = \beta h_1 = \frac{2\pi f h_1}{c}. \tag{5}$$

Therefore, we can get

$$|Q|^2 = M^2\cos^2(\theta) + N^2\sin^2(\theta). \tag{6}$$

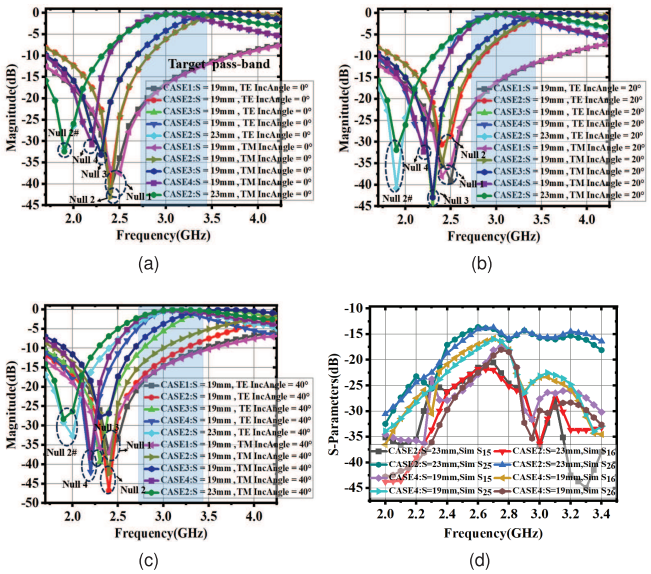

Fig. 9. Transmission coefficients under (a) normal incidence, (b) 20° incidence, (c) 40° incidence for different cases, and (d) mutual coupling coefficient in the adjacent frequency antenna (unit cell) when the LB element adopts CASE2: S = 23 mm or CASE4: S = 19 mm.

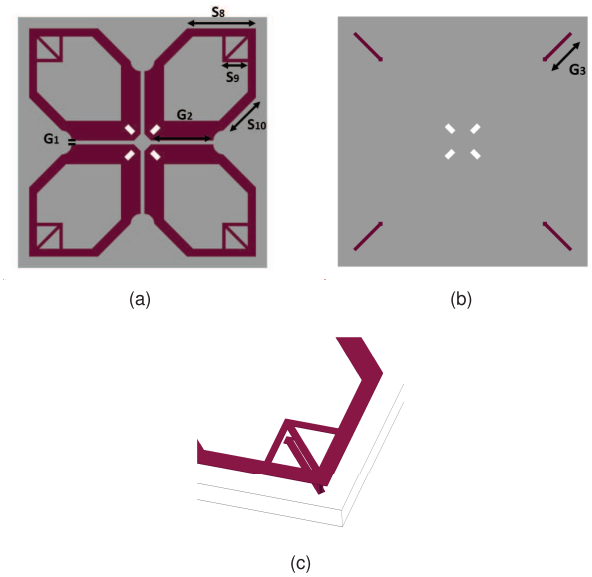

Fig. 10. Configuration of the proposed HB element. (a) Top view. (b) Bottom view. (c) EWG design.

TABLE I

OPTIMIZED DIMENSIONS OF THE PROPOSED ANTENNA (UNIT: mm)

D_0	D_1	D_2	H_0	H_1	H_2	S_0	S_1	S_2
68	65	100	10	18	30	19.7	10	14
S_3	S_4	S_5	S_6	S_7	S_8	S_9	S_{10}	G_0
10	4	2.1	1.4	2.8	10.5	3.86	6.2	0.1
G_1	G_2	G_3	L_0	L_1	L_2	L_3	L_4	L_5
0.6	7	10	1.55	2.5	1	4	4.6	8.5
L_6	L_7	L_8	L_9	L_{10}	L_{11}	L_{12}	L_{13}	L_{14}
11.3	2	7.1	6	3	6.5	4.7	6.75	2
L_{15}	L_{16}	L_{17}	L_{18}	L_{19}	L_{20}	W_0	W_1	
13	17.2	6.6	6	3	12.1	0.9	1.2	

We continue to derive θ in $|Q|^2$ and get

$$\frac{d|Q|^2}{d\theta} = \sin(2\theta)\left(N^2 - M^2\right). \tag{7}$$

From formula (7), we know that if the transfer function is bandpass, then $M = N$ does not exist. Therefore, assuming that there is a frequency f_1 as the transmission zero point, then the corresponding $d|Q|^2/d\theta = 0$, so we can know exists

$$sin(2\theta) = 0, f_1 h_1 = \frac{m_0 c}{4} \tag{8}$$

where m_0 is a constant integer. Therefore, according to formula (8), simply changing h_1 can significantly affect the position of the transmission zero point. The experiment shown in Fig. 9 shows that adding a 3-D choke will increase the wave propagation path, thereby increasing the transmission electrical length, and ultimately causing the transmission zero point to shift left from Null 2 to Null 3.

Therefore, in Fig. 8(d), we adopt the solution of Cases 2 and 3, the 3-D choke to shift the transmission zero to the left, and a special patch to shape FSS, introduce a new resonance, and shift the passband to the left. As shown in Fig. 9, we can clearly see the movement of the transmission zero and the realization of the target passband.

Other methods to increase the transmission electrical length include increasing the square ring length S or the dielectric thickness. Therefore, when we increase S from 19 to 23 mm in CASE2, it can achieve the same passband effect, but this will increase the overall area of LB element to 146.5% of the original and will seriously deteriorate the mutual coupling between the LB element and HB elements in the adjacent frequency antenna, as shown in Fig. 9(d).

Based on the above experiment, we finally designed the corresponding LB element. The key dimensions of the LB and HB elements are presented in Table I.

D. Design of The HB Element

Fig. 10 shows the patch structure of the HB element. The patches are all printed on the FR4 with a dielectric constant of 4 and a thickness of 0.762 mm, as shown in Fig. 10(a) and (b). The dipole arm is designed in a diamond shape. A semicircle is dug out of the curved part of the dipole arm, as shown in Fig. 10(a), to optimize the impedance matching.

At the same time, we add an extension wire to the end of the dipole arm, and the upper and lower parts of the patches are grounded through metal pins, as shown in Fig. 10(c) (EWG). Since the current at the end of the dipole arm is close to an open circuit, it can greatly reduce the coupling from the HB elements in the antenna (unit cell) as shown in Fig. 11. EWG can also optimize the impedance matching and increase resonance depth as shown in Fig. 9.

Due to the proximity of the frequency bands for the HB and LB elements, we find that there is a serious common-mode interference problem in this adjacent frequency antenna (unit

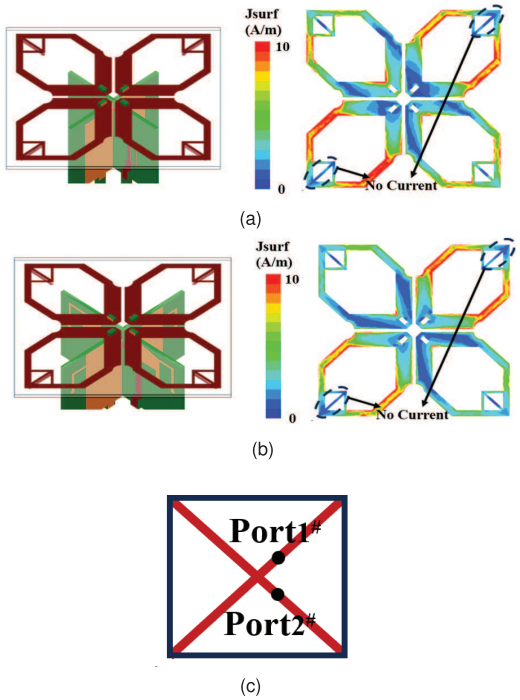

Fig. 11. Configuration and current distribution of HB elements (a) with conventional balun feeding and (b) with front feeding when exciting Port 1# at 3.1 GHz. (c) Port number assignment.

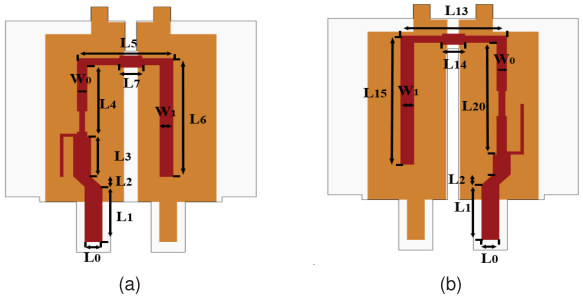

Fig. 12. Configuration of conventional balun feeding. (a) Balun1 design. (b) Balun2 design.

cell) when using the conventional balun feeding as shown in Fig. 12. In our experiments, we find that the radiation pattern of the LB component will be seriously affected by the HB component, resulting in distortion. To address this issue, we design a new feeding method for the HB element as shown in Fig. 13, a feeding structure where energy is transferred to the radiating surface through a slot line on the front side, which is connected to the slot line on the back side. Both the slot lines on the front and back sides are connected to the metal pin through extended metal arms (EMAs). This design structure suppresses the coupling current generated by LB coupling while maintaining HB performance, thus achieving effective decoupling.

To verify the superiority of the front-feeding structure in this adjacent frequency antenna (unit cell), a simulation experiment was conducted to compare it with the conventional balun-feeding structure.

The similarity of the simulated S-parameters and Z-parameters shown in Figs. 14 and 15 indicates that

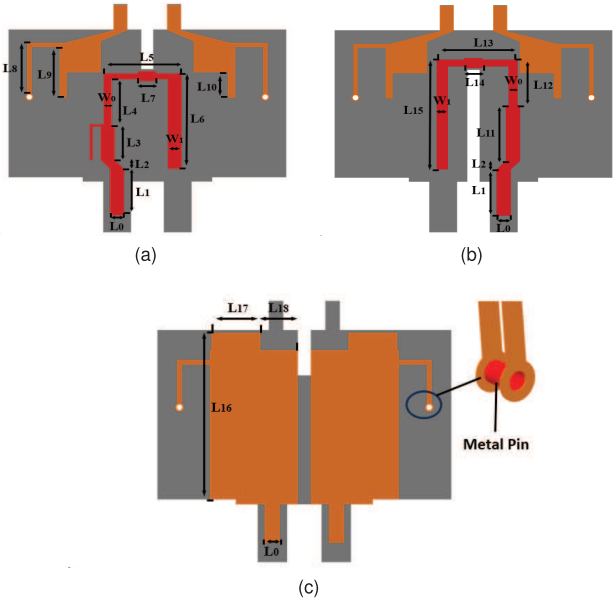

Fig. 13. Configuration of the proposed front-feeding. (a) Balun1 design front side. (b) Balun2 design front side. (c) Balun design back side.

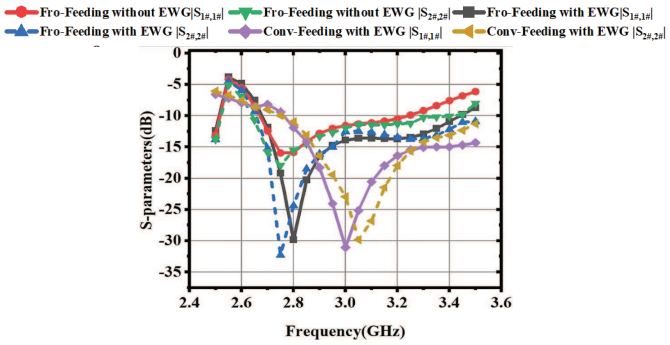

Fig. 14. Simulated S-parameters on HB elements with front feeding and conventional balun feeding of Ports 1# and 2#.

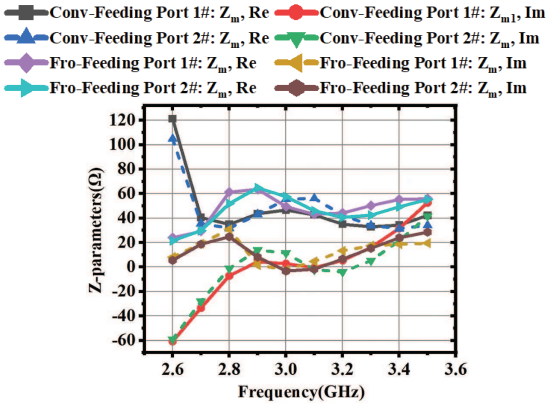

Fig. 15. Simulated Z-parameters on HB elements with front feeding and conventional balun feeding of Ports 1# and 2#.

the conventional balun feeding and the proposed front-feeding designs can be meaningfully compared experimentally. At the same time, we can see that using the front-feeding structure can have a better resonance depth and a smoother impedance transformation.

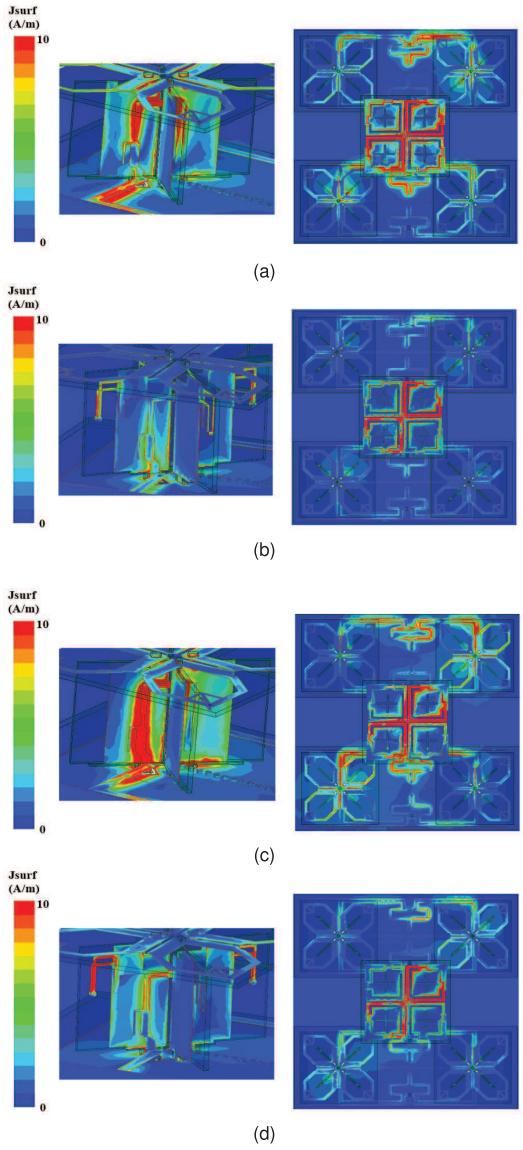

Fig. 16. Current distributions on the HB balun when the LB is excited. (a) Conventional balun feeding (2.1 GHz), (b) proposed front feeding (2.1 GHz), (c) conventional balun feeding (2.3 GHz), and (d) proposed front feeding (2.3 GHz).

When the LB element is excited in this unit cell, the schematic of the different currents for HB is presented in Fig. 16. We can clearly observe that the coupling current at 2.1 and 2.3 GHz is nearly eliminated when the HB uses the proposed front-feeding structure and the coupling current on the HB element radiation surface is also reduced, achieving the decoupling function.

We can better understand the principle of front-feeding structure decoupling from the circuit aspect. The classic band-stop filter structure is shown in Fig. 17. A simple and general approach for the design of band-stop filters is based on reactance slope parameters of the resonators. The transition from low-pass to band-stop characteristics can be obtained by

$$\Omega = \frac{\Omega_c \mathrm{FBW}}{(\omega/\omega_0 - \omega_0/\omega)} \tag{9}$$

$$\omega_0 = \sqrt{\omega_1 \omega_2} \tag{10}$$

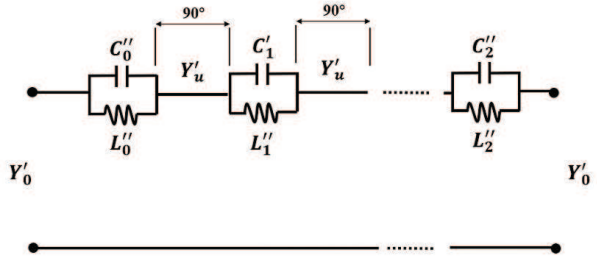

Fig. 17. Classic band-stop filter structure.

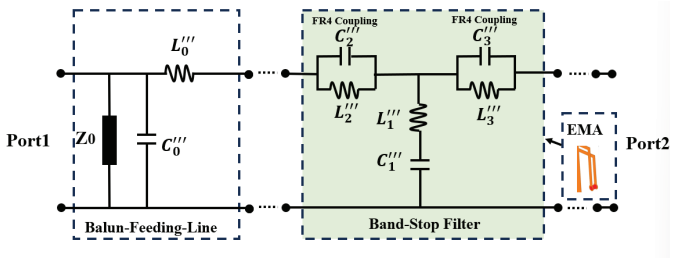

Fig. 18. Approximate equivalent circuit of front feeding.

$$\mathrm{FBW} = \frac{\omega_2 - \omega_1}{\omega_0} \tag{11}$$

where Ω is the normalized frequency variable of a low-pass prototype; Ω_c is its cutoff; and ω_0 and FBW are the mid-band frequency and fractional bandwidth of the band-stop filter, respectively. Also, the circuit satisfies

$$\left(\frac{Y_U}{Y_0}\right)^2 = \frac{1}{g_0 g_{n+1}} \tag{12}$$

$$b_i = \omega_0 C_i = \frac{1}{\omega_0 L_i} = Y_0 \left(\frac{Y_U}{Y_0}\right)^2 \frac{g_0}{g_i \Omega_c \mathrm{FBW}} \quad \text{for} \quad i = 1 \text{ to } n \tag{13}$$

where b_i is the susceptance slope parameter of series–parallel resonators. It is obvious that for a chosen low-pass prototype, with known element values, the desired reactance slope parameters can easily be determined using (11) and (12). The next step is to design microwave band-stop resonators so as to have prescribed slope parameters. To derive the formulation for extracting the susceptance slope parameter, let us consider a two-port network with a single series branch of $Y = j\omega C + 1/j\omega L$, such as the one in Fig. 13. The series branch has a parallel-resonant frequency $\omega_0 = 1/LC$ and a susceptance slope parameter $b = \omega_0 C$. The transmission parameter for this two-port network terminated with Y_0 is given by

$$|S_{21}| = \frac{1}{\sqrt{1 + \left[\frac{1}{4(x/Z_0)} \frac{\omega_0}{\Delta\omega}\right]^2}} \tag{14}$$

where $(\omega/\omega_0 - \omega_0/\omega) \approx 2\Delta\omega/\omega_0$ using $\omega = \omega_0 + \Delta\omega$. This is at resonance when $\omega = \omega_0$ or $\Delta\omega = 0$, and $|S_{21}| = 0$ because the resonant series branch blocks out the transmission and causes an attenuation pole. The attenuation will then be reduced or

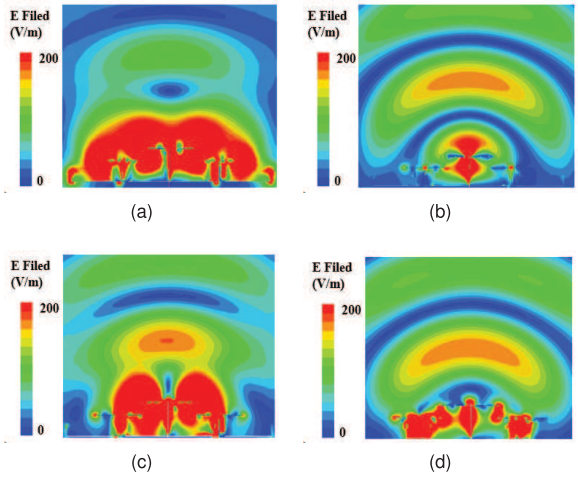

Fig. 19. Simulated E-field when the LB is excited. (a) Conventional balun feeding (2.1 GHz), (b) proposed front feeding (2.1 GHz), (c) conventional balun feeding (2.3 GHz), and (d) proposed front feeding (2.3 GHz).

the value of $|S_{21}|$ will rise when the frequency shifts away from ω_0. When the frequency shifts such that

$$\frac{1}{4\,(b/Y_0)}\frac{\omega_0}{\Delta\omega_{\pm}} = \pm 1. \tag{15}$$

Therefore, we have

$$\left(\frac{b}{Y_0}\right) = \frac{\omega_0}{2\Delta\omega_{3\text{dB}}} = \frac{f_0}{2\Delta f_{3\text{dB}}}. \tag{16}$$

In the approximate equivalent circuit of front feeding as shown in Fig. 18, Port 1 indicates the direction of energy flowing from the input end to the antenna radiation surface, while Port 2 represents the direction of energy radiating from the antenna surface and any other energy coupling into the system.

One aspect that needs to be focused on is the EMA structure. This structure ensures that the energy can be transmitted from the exciting port to the radiating surface not only through electromagnetic coupling through the FR4 medium but also through the EMA itself.

In this structure, we can equate the energy transmission through the FR4 electromagnetic coupling to the parallel connection of parasitic capacitance and inductance, and the EMA structure to an *LC* series circuit. Therefore, this part can be equivalent to a third-order band-stop filter, and the length of the EMA structure should be 1/4 wavelength of the center frequency of the corresponding band-stop frequency band. After experimental verification, the 1/4 wavelength of the EMA structure corresponding to 2 GHz is the best choice. When the LB element is excited, the EMA structure can act as a band-stop filter and resonate in the target frequency band. This resonance helps to keep the energy within the EMA structure and minimize unnecessary coupling.

It is clearly visible in the surface current distribution and electric field distribution of Figs. 16 and 19 that the adjacent frequency antenna (unit cell) benefits from the front-feeding structure. The EMA structure can be seen in Fig. 16(b) and (d) to form the band-stop filter, which effectively suppresses the common-mode current compared to the traditional balun feeding of Fig. 16(a) and (c), which restored the electric field as shown in Fig. 19. To better integrate the antennas, we consider the adjacent frequency bands. The HB element causes significant coupling to the LB antenna when using a T-row power divider. Therefore, we design the following Wilkinson power divider printed on the FR4 with a dielectric constant of 4 and a thickness of 1 mm, as shown in Fig. 20.

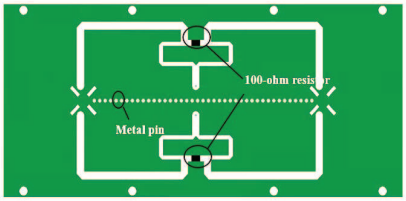

Fig. 20. Wilkinson power divider for HB element.

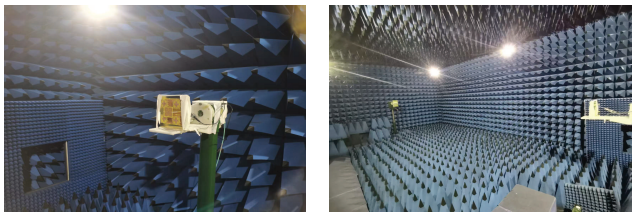

Fig. 21. (a) Practical antenna and (b) measurement scenario.

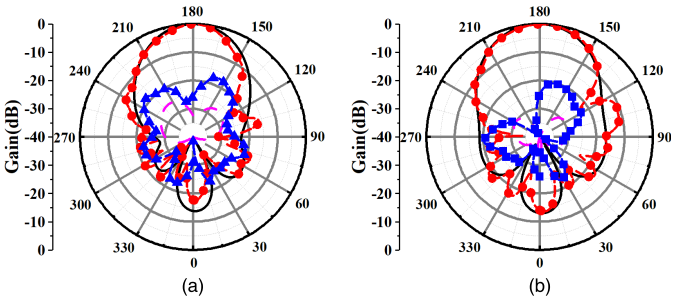

Fig. 22. Simulated and measured radiation patterns for the LB element when Port 5 is excited. E-plane at (a) 2.1 and (b) 2.5 GHz.

TABLE II

COMPARISON OF THE PROPOSED ANTENNA WITH THE EXISTING ANTENNAS

Ref.	Bandwidth (GHz)	Gain (dBi)	Isolation (dB)	Height (λ_0)
[5]	0.69-0.96 3.3-3.8	LB: 8.6±0.6 ; HB: 8.1±0.4	>38 >25	0.25
[6]	0.698-0.96 1.7-2.7	LB: 11.15±0.65 ; HB: 14.65±0.95 (2 × 5arrays)	>24 >29	0.44
[8]	0.69-0.96 3.3-3.8	LB: 9±0.3; HB: 8.3±0.7	>20 >15	0.53
[16]	1.8-2.7 3.3-3.8	LB: 7.2±0.9; HB: 8.6±1.3	>20 >20	0.24
This work	2.0-2.6 2.7-3.4	LB: 8.3±0.5 HB: 13±0.7 (1 × 4 arrays)	>25 >20	0.23

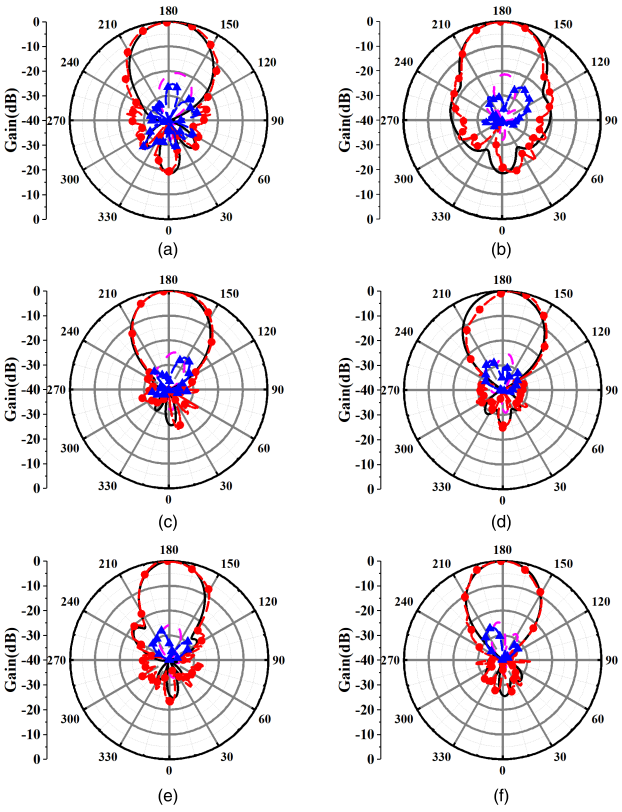

Fig. 23. Simulated and measured radiation patterns for HB elements when Ports 1 and 3 are excited. E-plane at (a) 2.7, (c) 3.1, and (e) 3.4 GHz. H-plane at (b) 2.7, (d) 3.1, and (f) 3.4 GHz.

III. Adjacent Frequency Antenna Verification

We measure the overall performance of the adjacent frequency antenna array, as shown in Figs. 21. Figs. 22 and 23 indicate that the E-plane cross-polarization discriminations (XPDs) for the LB element are below −20 dB at 2.1 and 2.5 GHz. In contrast, the E-plane XPDs for the HB element are below −25 dB at 2.7, 3.1, and 3.4 GHz.

As illustrated in Fig. 24, the return loss for the LB element is less than −10 dB in the target frequency range of 2.0–2.6 GHz, with an isolation exceeding 25 dB. Likewise, the return loss for the HB antenna is also below −10 dB in the frequency range of 2.7–3.4 GHz, and its isolation is better than 20 dB. Fig. 24 shows a high gain of 8.3 ± 0.5 dBi in the LB element is obtained, with an average increase of 1.1 dBi using front feeding compared to conventional balun feeding, and a high gain of 13 ± 0.7 dBi in HB elements is obtained. At the same time, we can see that the isolation between HB and LB elements is better than 17 dB, which has a very low coupling characteristic. In Fig. 24, it is evident that the adjacent frequency antenna (unit cell) benefits from a front-feeding structure, which increases the gain by an average of 1.1 dBi in the target frequency band compared to the conventional balun-feeding method. Additionally, the gain and bandwidth of this configuration are more comparable to those of the LB placed alone.

As can be seen from Table II, the proposed 3D-FSS for LB element and EMA for HB elements can achieve effective cross-band decoupling in the low-profile scenario within the adjacent frequency band. The verification results show that the 3D-

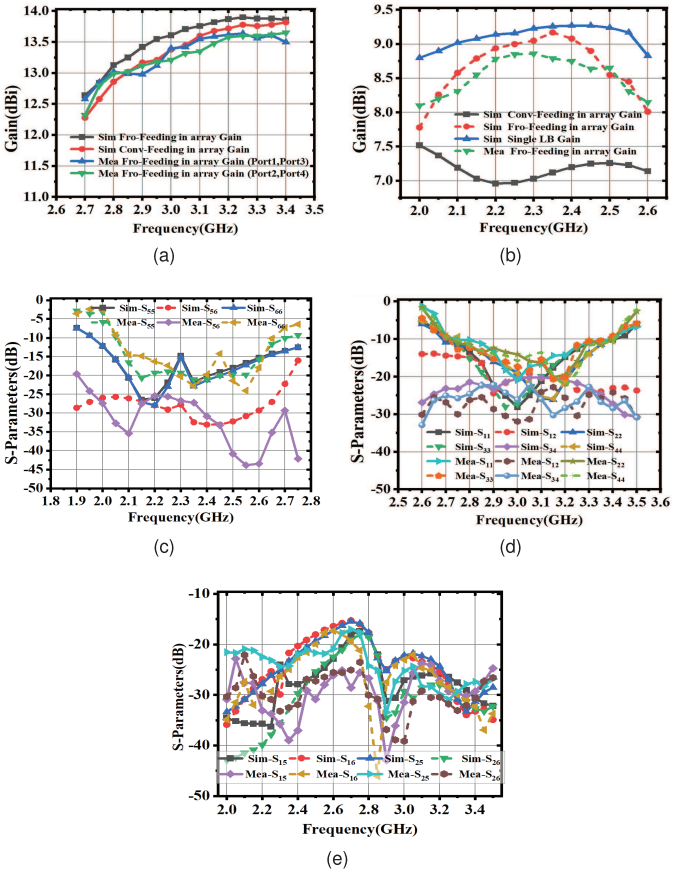

Fig. 24. Simulated and measured gain for (a) HB elements (Ports 1, 3 are excited) and (b) LB element (Port 5 is excited), (c) S-parameters for LB element (Port 5), (d) S-parameters for HB elements (Ports 1, 3), and (e) S-parameters for mutual coupling coefficient.

FSS structure suppresses differential-mode interference, while the EMA structure suppresses common-mode interference, highlighting that both components are indispensable.

IV. Conclusion

This article presents the design of a 3D-FSS and a front-feeding structure aimed at decoupling the primary antenna. Given the close frequency bands involved, it is essential to minimize coupling between the higher frequency and lower frequency signals simultaneously. The proposed structures effectively achieve decoupling of lower frequency from higher frequency and vice versa. Simulated and measured results demonstrate that the proposed antenna (unit cell) exhibits excellent impedance matching, high polarization isolation, and effective cross-band isolation. It also shows a stable radiation pattern and suppression of cross-band coupling in the lower frequency range of 2.0–2.6 GHz and the higher frequency range of 2.7–3.4 GHz. Consequently, this proposed antenna is suitable for use as a dual-band shared-aperture base station antenna array for a 5G mobile communication system. Although the proposed base station antenna comprises only one LB antenna and four HB antennas, further research can be conducted on the additional array by selecting various unit cell combinations. This flexibility allows for the reconfiguration of multiband or full-spectrum access base station antennas with respect to frequency, bandwidth, and radiation patterns.

REFERENCES

[1] Y. He, W. Huang, Z. He, L. Zhang, X. Gao, and Z. Zeng, "A novel cross-band decoupled shared-aperture base station antenna array unit for 5G mobile communications," *IEEE Open J. Antennas Propag.*, vol. 3, pp. 583–593, 2022.

[2] Y. He, Z. Pan, X. Cheng, Y. He, J. Qiao, and M. M. Tentzeris, "A novel dual-band, dual-polarized, miniaturized and low-profile base station antenna," *IEEE Trans. Antennas Propag.*, vol. 63, no. 12, pp. 5399–5408, Dec. 2015.

[3] F. Jia, S. Liao, and Q. Xue, "A dual-band dual-polarized antenna array arrangement and its application for base station antennas," *IEEE Antennas Wireless Propag. Lett.*, vol. 19, pp. 972–976, 2020.

[4] L. Y. Nie et al., "A low-profile coplanar dual-polarized and dual-band base station antenna array," *IEEE Trans. Antennas Propag.*, vol. 66, no. 12, pp. 6921–6929, Dec. 2018.

[5] Y. Li and Q.-X. Chu, "Coplanar dual-band base station antenna array using concept of cavity-backed antennas," *IEEE Trans. Antennas Propag.*, vol. 69, no. 11, pp. 7343–7354, Nov. 2021.

[6] R. Wu and Q.-X. Chu, "A compact, dual-polarized multiband array for 2G/3G/4G base stations," *IEEE Trans. Antennas Propag.*, vol. 67, no. 4, pp. 2298–2304, Apr. 2019.

[7] Y. Li and Q.-X. Chu, "Shared-radiator design of dual-band coplanar base station antenna array using cavity-backed slots," *IEEE Trans. Antennas Propag.*, vol. 69, no. 12, pp. 8985–8990, Dec. 2021.

[8] H. Li, J. Xu, Y. Nan, Q. Chen, and C. Zhou, "Low-profile dual-band shared-aperture base station antennas based on FSS radiators," *IEEE Antennas Wireless Propag. Lett.*, vol. 23, pp. 1894–1898, 2024.

[9] S. J. Yang, W. Duan, Y. Y. Liu, H. Ye, H. Yang, and X. Y. Zhang, "Compact dual-band base-station antenna using filtering elements," *IEEE Trans. Antennas Propag.*, vol. 70, no. 8, pp. 7106–7111, Aug. 2022.

[10] Y. Chen, J. Zhao, and S. Yang, "A novel stacked antenna configuration and its applications in dual-band shared-aperture base station antenna array designs," *IEEE Trans. Antennas Propag.*, vol. 67, no. 12, pp. 7234–7241, Dec. 2019.

[11] J. Yin, Y. Jia, S. Yang, and H. Zhai, "Design of a composite decoupling structure for dual-band dual-polarized base station array," *IEEE Antennas Wireless Propag. Lett.*, vol. 21, pp. 1408–1412, 2022.

[12] P. Liu, F. Jia, Y. Zhang, G. Su, Q. Wang, and X. Y. Zhang, "Dual-polarized dipole antenna with dual-band spatial filtering response for aperture-shared triband base station array application," *IEEE Antennas Wireless Propag. Lett.*, vol. 22, pp. 3057–3061, 2023.

[13] Z. Chen, T. Xu, J.-F. Li, L. H. Ye, and D.-L. Wu, "Dual-broadband dual-polarized base station antenna array with stable radiation pattern," *IEEE Antennas Wireless Propag. Lett.*, vol. 22, pp. 303–307, 2023.

[14] R. Li, Y. Zhang, B. Xiao, and Y. Cui, "An aperture-shared dual-band antenna array based on upstanding dipoles," *IEEE Antennas Wireless Propag. Lett.*, vol. 22, pp. 2675–2679, 2023.

[15] Y. Fan, Y. Cheng, and Y. Dong, "A wideband shared-aperture dual-band base station antenna array based on inhomogeneous metasurface," *IEEE Antennas Wireless Propag. Lett.*, vol. 23, pp. 463–467, 2024.

[16] D. He, Q. Yu, Y. Chen, and S. Yang, "Dual-band shared-aperture base station antenna array with electromagnetic transparent antenna elements," *IEEE Trans. Antennas Propag.*, vol. 69, no. 9, pp. 5596–5606, Sep. 2021.

[17] J.-X. Chen, X.-F. Wang, L.-L. Yang, X.-R. Wang, X.-F. Gu, and W.-W. Yang, "Asymmetrical low-RCS FSS-based antenna for tri-band shared-aperture array," *IEEE Antennas Wireless Propag. Lett.*, vol. 23, pp. 1563–1567, 2024.

[18] H.-H. Sun, H. Zhu, C. Ding, B. Jones, and Y. J. Guo, "Scattering suppression in a 4G and 5G base station antenna array using spiral chokes," *IEEE Antennas Wireless Propag. Lett.*, vol. 19, pp. 1818–1822, 2020.

[19] J. Jiang and Q.-X. Chu, "Dual-band shared-aperture base station antenna array based on 3-D chokes," *IEEE Antennas Wireless Propag. Lett.*, vol. 22, pp. 824–828, 2023.

[20] W. Niu, B. Sun, G. Zhou, and Z. Lan, "Dual-band aperture shared antenna array with decreased radiation pattern distortion," *IEEE Trans. Antennas Propag.*, vol. 70, no. 7, pp. 6048–6053, Jul. 2022.

[21] H.-H. Sun, C. Ding, H. Zhu, B. Jones, and Y. J. Guo, "Suppression of cross-band scattering in multiband antenna arrays," *IEEE Trans. Antennas Propag.*, vol. 67, no. 4, pp. 2379–2389, Apr. 2019.

[22] J. H. Zhai, Y. F. Cao, Q. Xue, and W. Che, "Cross-band decoupling method for dual-band aperture-shared antenna array using metasurfaces," *IEEE Trans. Antennas Propag.*, vol. 72, no. 2, pp. 2001–2006, Feb. 2024.

[23] Y.-L. Chang and Q.-X. Chu, "Suppression of cross-band coupling interference in tri-band shared-aperture base station antenna," *IEEE Trans. Antennas Propag.*, vol. 70, no. 6, pp. 4200–4214, Jun. 2022.

Yejun He (Senior Member, IEEE) received the Ph.D. degree in information and communication engineering from the Huazhong University of Science and Technology (HUST), Wuhan, China, in 2005.

From 2005 to 2006, he was a Research Associate with the Department of Electronic and Information Engineering, The Hong Kong Polytechnic University, Hong Kong. From 2006 to 2007, he was a Research Associate with the Department of Electronic Engineering, Faculty of Engineering, The Chinese University of Hong Kong, Hong Kong. In 2012, he joined the Department of Electrical and Computer Engineering, University of Waterloo, Waterloo, ON, Canada, as a Visiting Professor. From 2013 to 2015, he was an Advanced Visiting Scholar (Visiting Professor) with the School of Electrical and Computer Engineering, Georgia Institute of Technology, Atlanta, GA, USA. From 2023 to 2024, he was an Advanced Research Scholar (Visiting Professor) with the Department of Electrical and Computer Engineering, National University of Singapore, Singapore. Since 2006, he has been a Faculty of Shenzhen University, Shenzhen, China, where he is currently a Full Professor with the College of Electronics and Information Engineering, the Director of the Sino-British Antennas and Propagation Joint Laboratory of Ministry of Science and Technology of China (MOST), the Director of Guangdong Engineering Research Center of Base Station Antennas and Propagation, and the Director of Shenzhen Key Laboratory of Antennas and Propagation. He was selected as an Expert with Special Government Allowance from the State Council in China and a Leading Talent in "Guangdong Special Support Program" in 2024. He was promoted to Shenzhen "Pengcheng Scholar" Distinguished Professor in 2020. He has authored or co-authored more than 350 refereed journals and conference papers and seven books. He holds more than 30 patents. His research interests include wireless communications, antennas, and radio frequency.

Dr. He is a fellow of IET and China Institute of Communications (CIC). He was a recipient of Shenzhen Overseas High-Caliber Personnel Level B (Peacock Plan Award B) and Shenzhen High-Level Professional Talent (Local Leading Talent). He received the Second Prize of Shenzhen Science and Technology Progress Award in 2017, the Third Prize of Guangdong Provincial Science and Technology Progress Award in 2018, the Second Prize of Guangdong Provincial Science and Technology Progress Award in 2023, and the Tenth Guangdong Provincial Patent Excellence Award in 2023. He is currently the Chair of the IEEE Antennas and Propagation Society-Shenzhen Chapter and received the 2022 IEEE APS Outstanding Chapter Award. He has served as a Technical Program Committee Member or the Session Chair for various conferences, including the IEEE Global Telecommunications Conference (GLOBECOM), the IEEE International Conference on Communications (ICC), the IEEE Wireless Communication Networking Conference (WCNC), and the IEEE Vehicular Technology Conference (VTC). He served as the TPC Chair for IEEE ComComAp 2021 and the General Chair for IEEE ComComAp 2019. He was selected as a Board Member of the IEEE Wireless and Optical Communications Conference (WOCC). He served as the TPC Co-Chair for WOCC 2023/2022/2019/2015, APCAP 2023, UCMMT 2023, ACES-China2023, and NEMO 2020. He acted as the Publicity Chair of several international conferences, such as the IEEE PIMRC 2012. He has served as the Executive Chair for the 2024/2025 IEEE International Workshop on Radio Frequency and Antenna Technologies. He is the Principal Investigator for over 40 current or finished research projects, including the National Natural Science Foundation of China, the Science and Technology Program of Guangdong Province, and the Science and Technology Program of Shenzhen City. He has served as a reviewer for various journals, such as IEEE TRANSACTIONS ON VEHICULAR TECHNOLOGY, IEEE TRANSACTIONS ON COMMUNICATIONS, IEEE TRANSACTIONS ON INDUSTRIAL ELECTRONICS, IEEE TRANSACTIONS ON ANTENNAS AND PROPAGATION, IEEE WIRELESS COMMUNICATIONS, IEEE COMMUNICATIONS LETTERS, *International Journal of Communication Systems*, and *Wireless Personal Communications*. He is serving as an Associate Editor for IEEE TRANSACTIONS ON VEHICULAR TECHNOLOGY, IEEE TRANSACTIONS ON ANTENNAS AND PROPAGATION, IEEE TRANSACTIONS ON MOBILE COMPUTING, IEEE ANTENNAS AND WIRELESS PROPAGATION LETTERS, *IEEE Antennas and Propagation Magazine*, *International Journal of Communication Systems*, *China Communications*, and *ZTE Communications*.

Guodong Liao (Graduate Student Member, IEEE) is currently pursuing the master's degree in electronics and communication engineering with Shenzhen University, Shenzhen, China.

His research interests include base station antennas and microwave device auxiliary development.

Zhou He received the B.S. degree in electrical engineering from the University of Colorado Boulder, Boulder, CO, USA, in 2018. He is currently pursuing the Ph.D. degree in mechanical engineering with the University of Maryland, College Park, MD, USA.

His research interests include wireless communication, antennas, and reliability of electronic products.

Zhi Ning Chen (Fellow, IEEE) received the B.Eng., M.Eng., and Ph.D. degrees in electrical engineering from the Institute of Communications Engineering (ICE), China, in 1985, 1988, and 1993, respectively, and the second Ph.D. degree from the University of Tsukuba, Tsukuba, Japan, in 2003.

He has worked in academic, research organizations, and industry since 1988. He is currently a Provost Chair Professor and the Director of the Advanced Research and Technology Innovation Center, National University of Singapore, Singapore. He has been invited to deliver over 110 keynote, plenary, and invited speeches at international academic and industry events. He has published over 750 academic papers and seven books, as well as held over 36 granted/filed patents and completed over 42 technology licensing deals with industry. He is a pioneer in developing small and ultrawideband antennas, wearable/implanted medical antennas, package antennas, near-field antennas/coils, 3-D integrated LTCC arrays, and microwave metamaterial-metasurface antennas. Currently, he is focusing on the translational research of metasurfaces into antenna engineering as well as the development of algorithms, particularly machine learning-enabled synthesis methods for metantennas.

Dr. Chen was elevated to a fellow of the Academy of Engineering, Singapore, in 2019 and Asia-Pacific Artificial Intelligence Association (AAIA). He is serving as a member of the AdCom for the IEEE Antennas and Propagation Society from 2023 to 2025. He was a recipient of the EurAAP Antenna Award in 2025, the IEEE John Kraus Antenna Award in 2021, and many other academic and engineering awards. He is the Founding General Chair of several international workshops and symposiums, including the International Workshop on Antenna Technology (iWAT) in 2005, International Symposium on InfoComm and Mechatronics Technology in Bio-Medical and Healthcare Application (IS 3Tin3A) in 2010, International Microwave Forum (IMWF) in 2010, Asia-Pacific Conference on Antennas and Propagation (APCAP) in 2012, and Marina Forum (Mar-For) in 2021. He has also been involved in many international events as a general chair, a chair, and a member of technical program committees and international advisory committees. He is serving as the Vice President of AAIA. He served on the IEEE Council on RFID as a Vice President and a Distinguished Lecturer from 2015 to 2021, as well as on IEEE TRANSACTIONS ON ANTENNAS AND PROPAGATION as an Associate Editor from 2012 to 2018 and from 2023 to 2025 and the IEEE Antennas and Propagation Society as a Distinguished Lecturer from 2009 to 2012.